

## *Supporting Information*

# Interplay between CO disproportionation and oxidation: on the origin of the CO reaction onset on ALD-grown Pt/ZrO<sub>2</sub> model catalysts

*Verena Pramhaas<sup>a</sup>, Matteo Roiaz<sup>a</sup>, Noemi Bosio<sup>b</sup>, Manuel Corva,<sup>d,c</sup> Christoph Rameshan<sup>a</sup>,  
Erik Vesselli<sup>c,d</sup>, Henrik Grönbeck<sup>b</sup>, Günther Rupprechter<sup>a,\*</sup>*

<sup>a</sup>Institute of Materials Chemistry, Technische Universität Wien, Vienna, 1060, Austria

<sup>b</sup>Department of Physics and Competence Centre for Catalysis, Chalmers University of  
Technology, Gothenburg, 41296, Sweden

<sup>c</sup>Department of Physics, University of Trieste, via Valerio 2, 34127 – Trieste, Italy

<sup>d</sup>IOM-CNR Laboratorio TASC, Area Science Park – SS 14 km 163.5, 34149 Basovizza  
(Trieste), Italy

\*Corresponding author (guenther.rupprechter@tuwien.ac.at)

## 1. Model catalysts

### 1.1 Atomic Layer Deposition (ALD) Process and ALD Pt samples

ALD is a chemical vapor deposition (CVD) process, alternatingly dosing precursors to form self-limiting layers on a surface<sup>1</sup>. It is therefore possible to deposit uniform monolayers per ALD cycle and to control film thickness by repeating cycles.

The precursors used for zirconia film deposition were tetrakisdimethylamido-zirconium  $\text{Zr}(\text{NMe}_2)_4$  and  $\text{H}_2\text{O}$ ,<sup>2</sup> and those for Pt islands/films were methylcyclopentadienyl-trimethylplatinum  $\text{MeCpPtMe}_3$  and  $\text{O}_2$ . The exact deposition processes of these precursors are described in the literature<sup>3</sup>.

Zirconia ALD films were grown on Si(100), with cycles carried out at a deposition temperature of 200°C. The cycles consist of 0.15 s pulse time of the Zr precursor, followed by 10 s pumping, 0.025 s  $\text{H}_2\text{O}$  exposure, and 10 s pumping. To obtain a 42 nm thick zirconia film, 400 cycles were applied (deposition rate of 0.105 nm per cycle).

Pt was deposited at 270°C with a pulse time of 1 s of the Pt precursor, followed by 3 s pumping, 2 s exposure to  $\text{O}_2$ , and 3 s pumping. Varying the number of deposition cycles from 5 to 250 cycles produced samples with Pt nanoparticles and islands of different size up to closed films. Based on deposition rates from literature<sup>3</sup>, the estimated film thickness is 10 and 30 nm for the 250 and 750 cycle films, respectively.

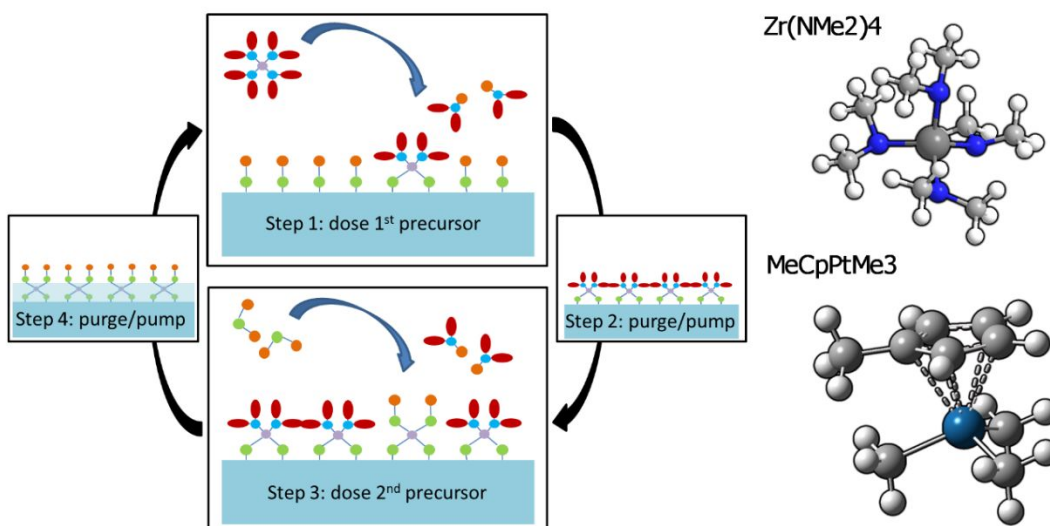


Figure S1: Illustration of the ALD process in 4 steps and of the two precursor molecules. In step 1, the first precursor (metal complex) is dosed. The complexes react with the active surface groups until the surface is covered with a full layer. The 2nd step is purging or pumping of the gas environment to hinder gas phase reactions. In the 3rd step, the second precursor is dosed, removing the rest of the ligands remaining from the metal complex and forming a new layer with re-established active end groups. In step 4, the gas phase is again purged/pumped to avoid gas phase reactions and disturbances in the self-limited process.

## 1.2 Pt single crystals

For reference, Pt(111) and (110) single crystals were used. The surfaces were prepared by standard cleaning procedures, i.e. cycles of 15-minute sputtering with  $1.5 \cdot 10^{-6}$  mbar Ar at room temperature and subsequent annealing to 800 °C for a clean and smooth surface.<sup>4</sup>

To achieve a slightly roughened surface the cleaned and annealed (111) single crystal was sputtered with Ar for 2 minutes without annealing.

### 1.3 Characterization: Electron Microscopy, X-ray diffraction, X-ray photoelectron spectroscopy

Scanning electron microscopy (SEM) on the 250 cycle films showed homogenous thin films (Fig. S2). The films with less Pt were not sufficiently conducting for SEM and were therefore imaged by transmission electron microscopy (TEM). For TEM, cross-sections were prepared (samples were glued head-on, followed by cutting lamellas and mechanical thinning/polishing), and bright-field as well as dark-field images were obtained (Fig. S3) to examine the structure and crystallites of the films. Up to 50 deposition cycles, individual Pt nanoparticles were observed, whereas more cycles produced continuous Pt films.

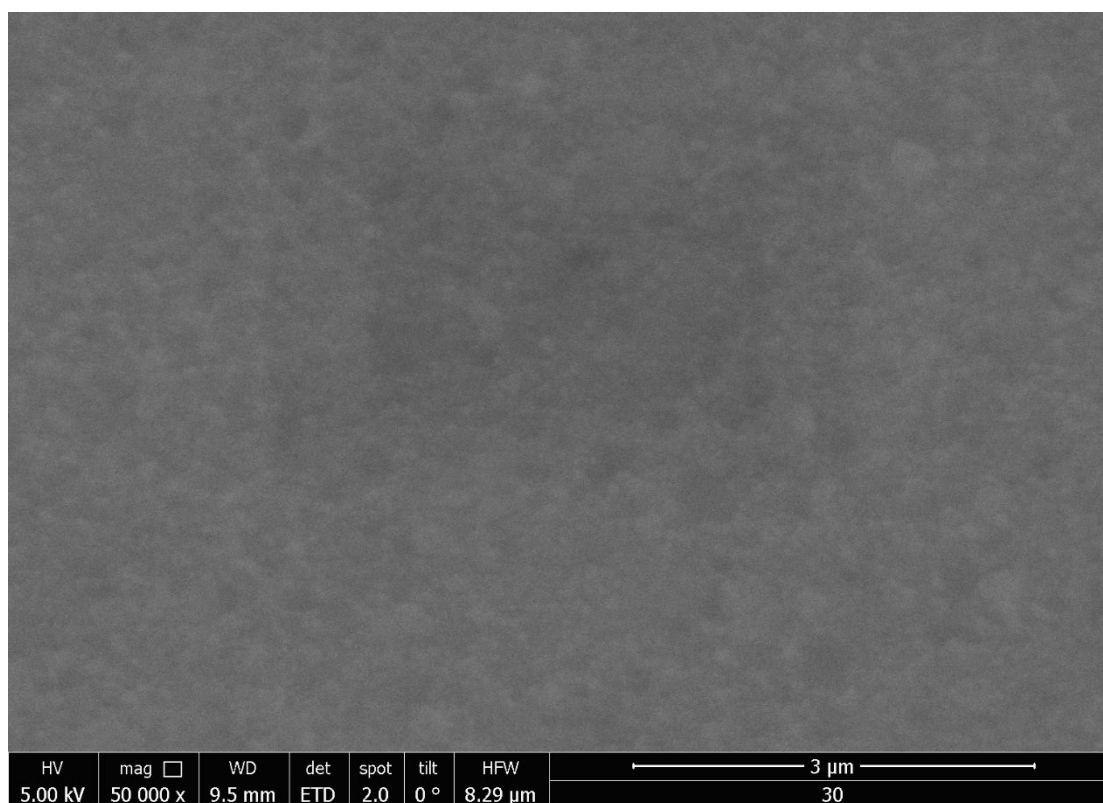


Figure S2: SEM of 250 cycle Pt film. A grainy structure can be observed, but no obvious imperfections are visible.

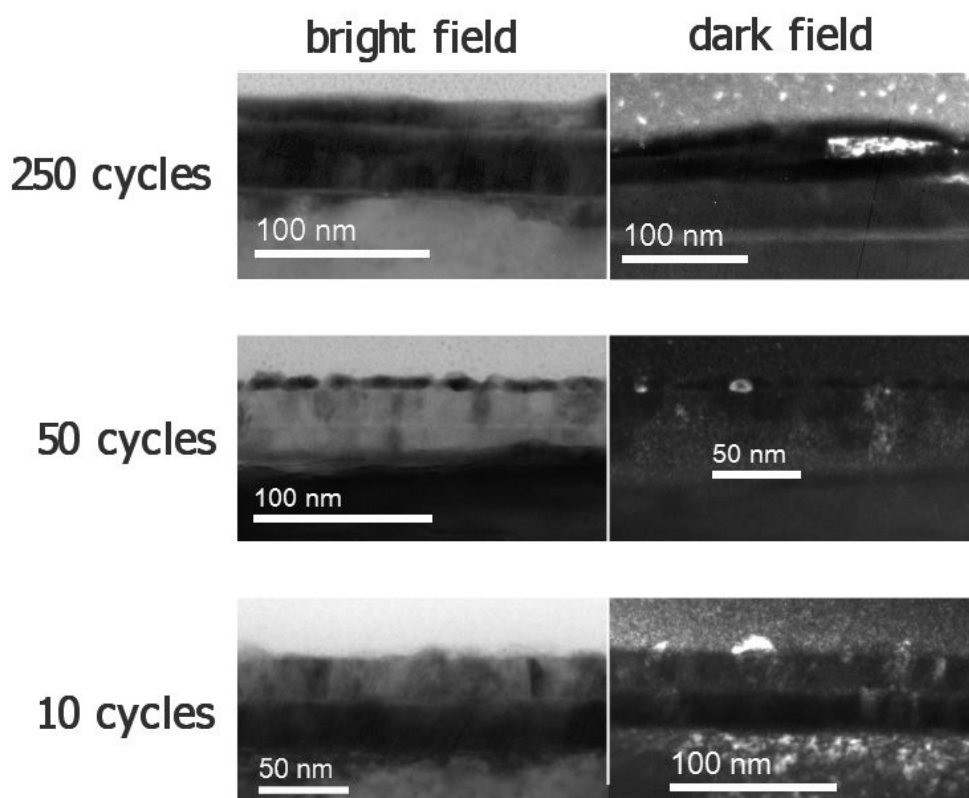


Figure S3: Bright- and dark-field TEM images of different samples, showing the cross section with the Si wafer at the bottom,  $\text{ZrO}_2$  made up of two 20 nm layers in the middle and the Pt film/particles on top. In dark-field, the size of some crystallites can be observed. For the particulate films, the crystallites are small, while for the closed film some large crystal sections were present.

X-Ray Diffraction (XRD) was used to investigate crystallinity of the deposited Pt and the zirconia film. The measurements were performed in standard powder diffraction measurement geometry, scanning along the angle  $\Theta$  within one plane. The measurements for the 50 and 250 cycle Pt films are shown in Fig S4.

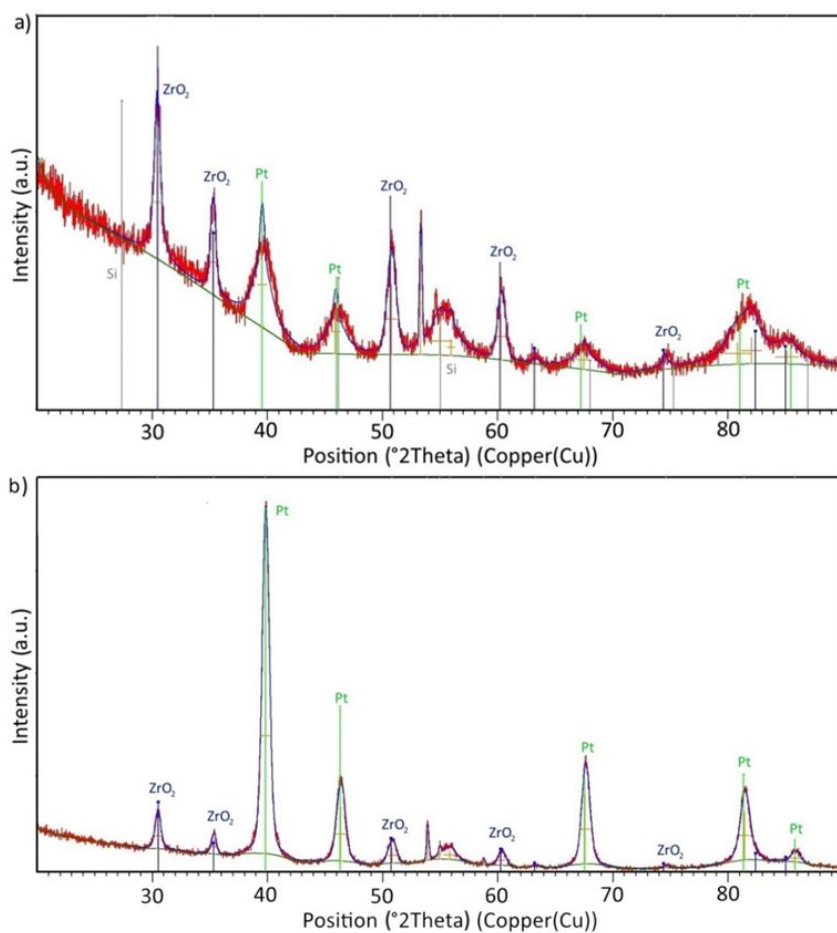


Figure S4: XRD data of a) 50 and b) 250 cycle Pt on 40 nm zirconia film.

Fitting X-ray diffraction data yielded a cubic lattice of the zirconia support with space group  $Fm\bar{3}m$  and a lattice spacing of  $a=b=c=5.11 \text{ \AA}$ . Based on the Scherrer equation, the mean crystal grain size was  $12.5 \pm 2.4 \text{ nm}$ . For Pt, XRD indicated a cubic  $Fm\bar{3}m$  lattice with spacing of  $a=b=c=3.92 \text{ \AA}$  and a mean crystallite size of  $9.8 \pm 1.4 \text{ nm}$  for the 250 cycle film, while the 50 cycle film shows strong peak broadening for the Pt features.

Figure S5 shows XPS spectra of the as-prepared Pt samples. The Pt 4f binding energy shifted to lower binding energies for more ALD cycles, as typically observed when metal nanoparticle size increases.

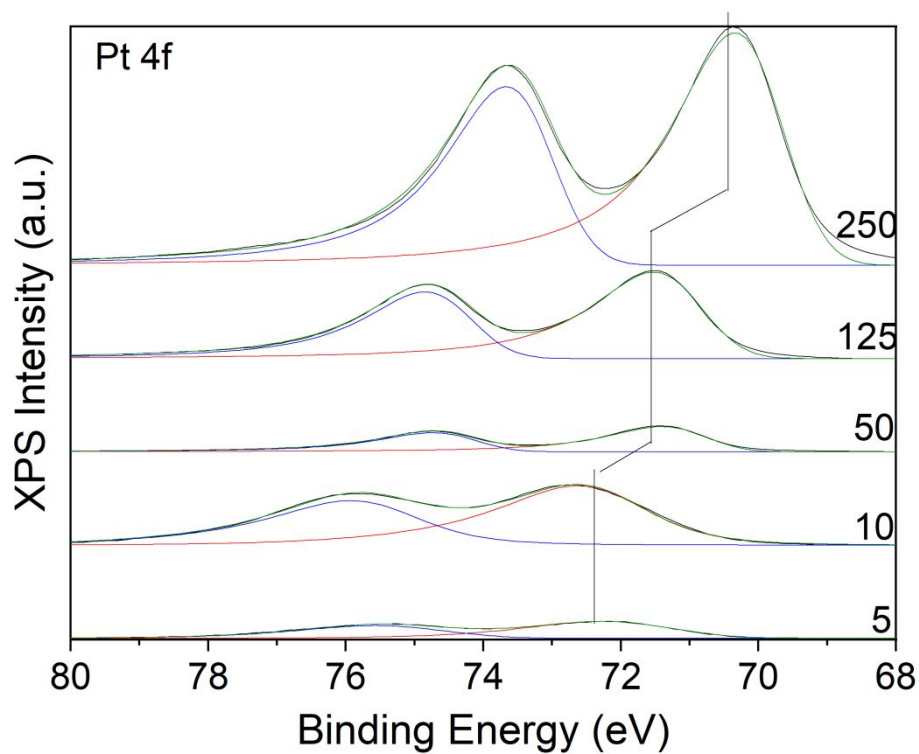


Figure S5: Pt 4f XPS spectra of different samples (Pt deposition cycles are denoted on the right). While clearly asymmetric lineshapes for metallic Pt are visible for large particles/continuous films, the two samples with few deposition cycles have the more symmetric peak structure typical for nanoparticles.

## 2. Operando Methods

For the presented measurements different measurement techniques were combined as illustrated in Fig. S6 for operando measurements.

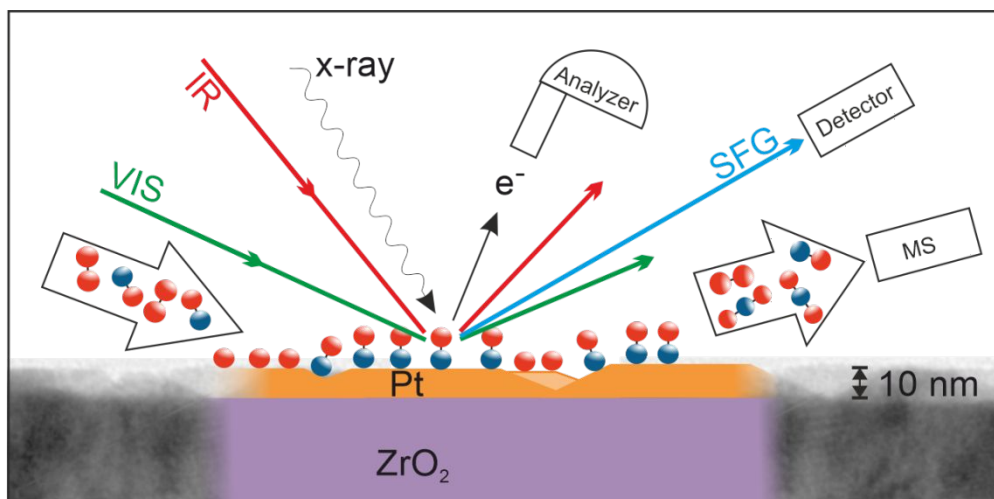


Figure S6: Schematic illustration of SFG, NAP-XPS and MS measurements during CO oxidation at mbar pressure. The samples consist of thin (e.g. 10 nm) Pt films on thicker (42 nm) zirconia films. The side panels show TEM images of a 250 ALD cycle Pt film on ZrO<sub>2</sub> with a modeled surface in-between. For SFG, two pulsed laser beams, one fixed at 532 nm (green) and one tunable in the IR (red), are overlapped on the sample and generate photons (blue) at the sum of the incident frequencies, providing vibrational spectra of adsorbed molecules. Synchrotron-based NAP-XPS was applied to the same model system. In both cases, the gas phase composition was simultaneously analyzed by a mass spectrometer (MS).

## 2.1 Sum Frequency Generation (SFG) Spectroscopy

SFG is based on a non-linear two-photon excitation, generating photons whose energy is the sum of the frequencies of the incident lasers<sup>5</sup>. Pulsed lasers are used to generate the high electric fields required to drive this non-linear interaction. For spectroscopic measurements, one laser is at constant visible wavelength (VIS: 532 nm) and the other is scanned in the mid infra-red (IR: 2.3-10 μm). When the IR light is in resonance with a vibrational excitation, the non-linear process is resonantly enhanced, expressed by the second order optical susceptibility  $\chi^{(2)}$ . The overall intensity depends on the intensities of both incident beams:

$$I_{\text{SFG}} \propto I_{\text{IR}} I_{\text{VIS}} \chi^{(2)}$$

with  $I_x$  denoting the respective pulse intensities and the second order nonlinear susceptibility  $\chi^{(2)}$  given as

$$\chi^{(2)} = A_{nr} e^{i\phi} + \sum \frac{A_{ri}}{\omega_{IR} - \omega_i - i\Gamma_i},$$

where  $A_{nr}$  is the off-resonant intensity,  $\phi$  is the phase difference,  $A_{ri}$  the peak intensity of resonance  $i$ ,  $\omega_i$  the position of resonance  $i$  and  $\Gamma_i$  its damping factor. The general susceptibility  $\chi^{(2)}$  is a tensor, so that the single elements measured in the lab depend on the used setup, i.e. the polarization of the incoming laser beams and the measured polarization of the SFG light. The standard measurement configuration for our model catalyst studies was p-polarization (parallel to plane of incidence) for all beams (Fig. S7).

For polarization-dependent measurements, the single polarizations of the beams are denoted as: "ppp", which stands for p-polarized SFG, p-polarized VIS and p-polarized IR beam, while "ssp" stands for s-polarized SFG, s-polarized VIS and p-polarized IR beam. The difference in SFG intensity for different polarization combinations strongly depends on the tilt angle of the probed bond, relative to the (macroscopic) surface normal.

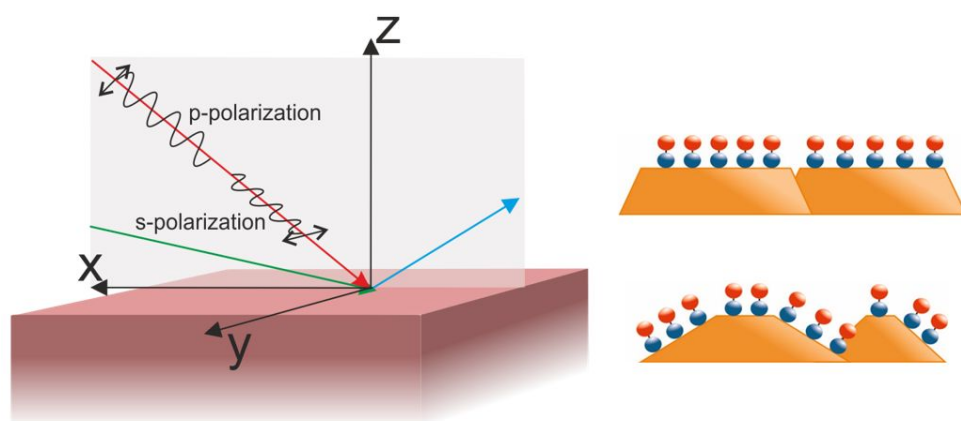


Figure S7: SFG coordinate system with x-z as plane of incidence. P-polarization oscillates in x and z direction, while s-polarization only oscillates in y direction, and models of CO adsorbed on Pt nanoparticles with flat top terrace and inclined side facets. CO is oriented perpendicular

to the surface. For flat surfaces most CO molecules are parallel to the (macroscopic) surface normal, while for rougher surfaces with inclined particle facets some CO molecules are tilted with respect to the macroscopic surface normal, causing an ssp signal in the SFG measurements.

A highly simplified explanation of this effect is obtained considering the electric fields of the beams. As seen in Fig. S7, p-polarization has an electric field in x and z direction, whereas s-polarization only oscillates in y direction. So, simplified, s-polarized beams cannot excite oscillations (e.g. stretching vibrations) parallel to the surface normal z that well. This means that for the CO-Pt system the ratio  $I_{\text{ppp}}/I_{\text{ssp}}$  drops with increasing tilt of the molecules within a certain range from the surface normal<sup>6</sup>. Detailed analysis of polarization-dependent SFG and intensity correlation to the tilt angle can be found in the literature<sup>7, 8</sup>. We also want to point the reader to SFG scattering theory for a detailed discussion<sup>9</sup>.

The used laser setup is based on a commercial SFG spectrometer (EKSPLA) (Fig. S8). It is comprised of a Nd:YAG laser at 1064 nm wavelength with a repetition rate of 50 Hz and a pulse length of 25 ps. A second harmonic generation unit produces the 532 nm VIS beam and an optical parametric generation & optical parametric amplification unit produces tunable infrared light from 2.3-10  $\mu\text{m}$ . The UHV preparation/characterization chambers and attached operando SFG high-pressure cell are described in detail in Roiaz et al.<sup>10</sup>. The adsorption/dissociation measurements comparing Pt(111) and the 250 cycle Pt film were carried out in a second similar SFG system (also from EKSPLA), described in ref<sup>11</sup>.

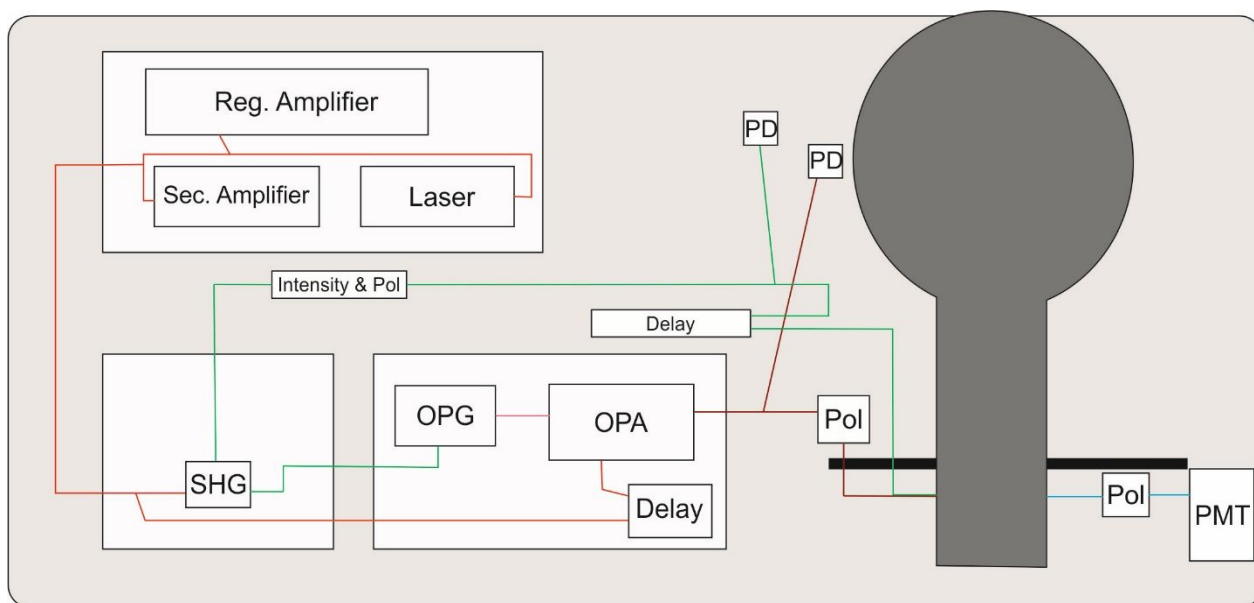


Figure S8: Spectroscopy setup for creating the IR and VIS pulsed laser beams and for measuring SFG spectra.

## 2.2 Near Ambient Pressure X-ray Photoelectron Spectroscopy (NAP-XPS)

XPS is a powerful surface science technique that yields information about surface composition and oxidation state<sup>12-14</sup>. For NAP-XPS strong differential pumping is applied in-between sample and analyzer, which enables measurements at mbar pressures. The current measurements were performed at the HIPPIE beamline at MAX IV in Lund, Sweden, which offers high beam brilliance and to select low photon energies, enabling more surface-sensitive spectroscopy.

## 3. Measurements of CO adsorption and dissociation

The pretreatment of the model catalyst surfaces consisted of repeated heating to 400°C in 10 mbar O<sub>2</sub> and subsequent heating to 300°C in 10 mbar CO/20 mbar O<sub>2</sub> mixture for 15 minutes. Temperature was controlled by a Ni/Ni-Cr thermocouple and a Eurotherm PID controller. For the temperature-dependent MS data, the heating ramp was 20°C/min.

To complement the Pt(111) and particle SFG measurements, Fig. S9 shows CO adsorption in 10 mbar CO on a Pt(110) crystal. The CO peak is red-shifted compared to Pt(111). Upon heating, the peak (irreversibly) loses intensity and shifts to lower wavenumbers. At 450 °C it is almost gone, but shows the typical line-shape change observed on the particle spectra upon reaching 275°C.

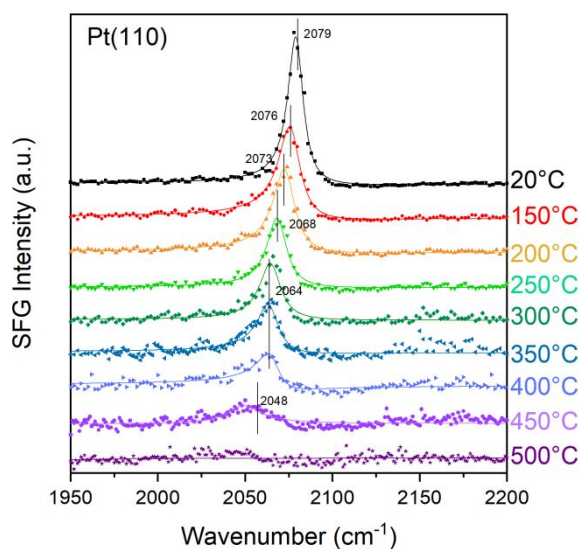


Figure S9: Temperature-dependent in-situ SFG spectra of 10 mbar CO on Pt(110). The CO signal keeps its normal line-shape up to 450 °C, where a slight deviation is observed.

### 3.1 CO orientation (SFG)

Polarization-dependent SFG was applied to determine the (macroscopic) bond orientation of adsorbed CO (note that microscopically CO adsorbs perpendicular on Pt surfaces). Accordingly, the comparison between ppp and ssp signals yields information on surface morphology. For rougher surfaces, there are facets inclined to the macroscopic surface normal and the adsorbed CO appears tilted. The CO molecules are still perpendicular to a facet, but tilted from the macroscopic surface normal, and then contribute to the ssp signal (Fig. S7).

The ratios of  $I_{\text{ppp}}/I_{\text{ssp}}$  from the spectra in Figure 1 and an additional measurement on the 10 cycle sample are given in Table S1.

Table S1: Fit values of Figure 1.

sample	$A_r/A_{nr}$ ppp	$A_r/A_{nr}$ ssp	$\omega$ (cm <sup>-1</sup> )	$\Gamma$	$\phi$ (rad)
250	0.277±0.005/	0.016±0.004/	2089±2	9.8±0.5	5.3±0.1
	0.0095±0.0002	0.0035±0.0001			
50	0.18±0.04/	0.061±0.005/	2086±2	9.7±0.5	5.7±0.2
	0.0058±0.0001	0.0066±0.0001			

Table S2: Intensity ratio of ppp to ssp SFG signals for the on-top CO peaks of different ALD Pt samples.

	250 cycle	50 cycle	10 cycle
Ratio $I_{\text{ppp}}/I_{\text{ssp}}$	17±4	2.4±0.5	3.4±1.0

### 3.2 CO dissociation (SFG)

When adsorption in 10 mbar CO was measured up to 225 °C, the spectra were fully reversible upon cooldown, as seen in Fig. S10a for the 250 cycle film. In contrast, after heating to 275 °C and cooldown to room temperature (Fig. S10b), the spectrum had low intensity, different line shape and also showed a 16 cm<sup>-1</sup> red-shift (different from CO/Pt(111)). Fig. S10c shows the analogous heating and cooldown measurement for the 50 cycle Pt sample, also confirming the irreversibility.

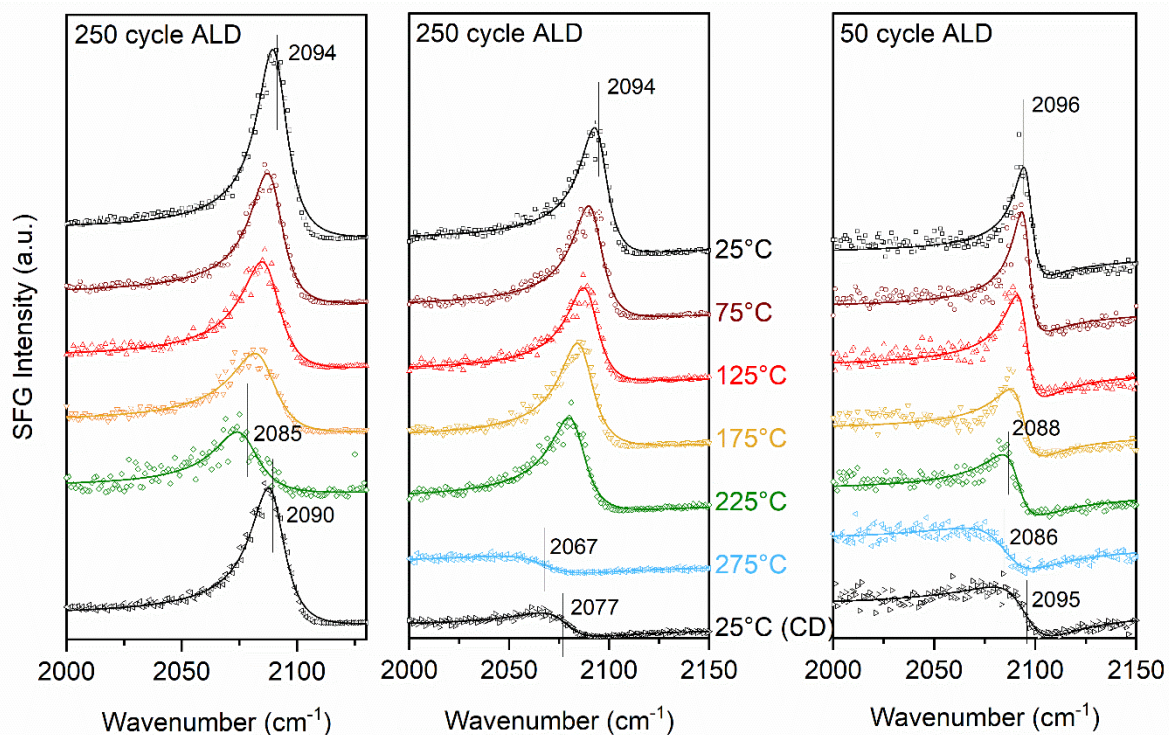


Figure S10: Temperature-dependent *in situ* SFG spectra in 10 mbar CO on 250 cycle ALD Pt/ZrO<sub>2</sub>: (a) Spectra measured (top to bottom) up to 225 °C were reversible. (b) Spectra measured up to up to 275 °C were not reversible after cooldown (CD). In (c), temperature-dependent *in situ* SFG spectra with the same irreversible change are shown for the 50 cycle ALD Pt film.

Table S3: Fit values for annealed Pt(111), 250 cycle ALD, 50 cycle ALD and sputtered Pt(111) for the spectra in Figure 2 and Figure S10.

Annealed Pt(111)				175 °C	225 °C	275 °C	
$\omega$ (cm <sup>-1</sup> ) $\pm 2$				2092	2084	2081	
$\Gamma$ (cm <sup>-1</sup> ) $\pm 0.5$				6.2	9.2	7.2	
$\Phi$ (rad) $\pm 0.2$				6.4	6.4	6.4	
250 cycle ALD	25 °C	75 °C	125 °C	175 °C	225 °C	275 °C	25 °C CD
$\omega$ (cm <sup>-1</sup> ) $\pm 2$	2094	2092	2090	2089	2085	2067	2077

$\Gamma$ (cm <sup>-1</sup> ) $\pm 0.5$	8.2	9.1	9.4	10.2	10.6	21.5	14.3
$\Phi$ (rad) $\pm 0.2$	6.2	6.1	6.2	6.1	6.3	6.9	6.6
<b>50 cycle ALD</b>	25 °C	75 °C	125 °C	175 °C	225 °C	275 °C	25 °C CD
$\omega$ (cm <sup>-1</sup> ) $\pm 2$	2096	2095	2094	2090	2088	2086	2095
$\Gamma$ (cm <sup>-1</sup> ) $\pm 0.5$	5.1	4.9	6.0	7.9	9.1	16.2	14.4
$\Phi$ (rad) $\pm 0.2$	6.1	6.1	6.4	6.5	6.5	6.8	6.8
<b>Sputtered Pt(111)</b>				175 °C	225 °C	275 °C	
$\omega$ (cm <sup>-1</sup> ) $\pm 2$				2081	2076	2047	
$\Gamma$ (cm <sup>-1</sup> ) $\pm 0.5$				10.7	11.2	17.4	
$\Phi$ (rad) $\pm 0.2$				6.3	6.7	6.4	

The irreversible change may be due to CO dissociation, leading to significant carbon poisoning of the surface. In this case, carbon should be removed by adding O<sub>2</sub>. The respective measurement in 10 mbar CO and 20 mbar O<sub>2</sub> is shown in Fig. S11. At 175 °C, a first shift and increase of the CO peak was observed. At 225 °C, the original CO signal was restored (the slight blue-shift may indicate an even higher CO coverage than in pure CO environment). The same removal of carbon-deposits was observed for heating the 50 cycle ALD Pt film in 10 mbar CO and 20 mbar O<sub>2</sub>.

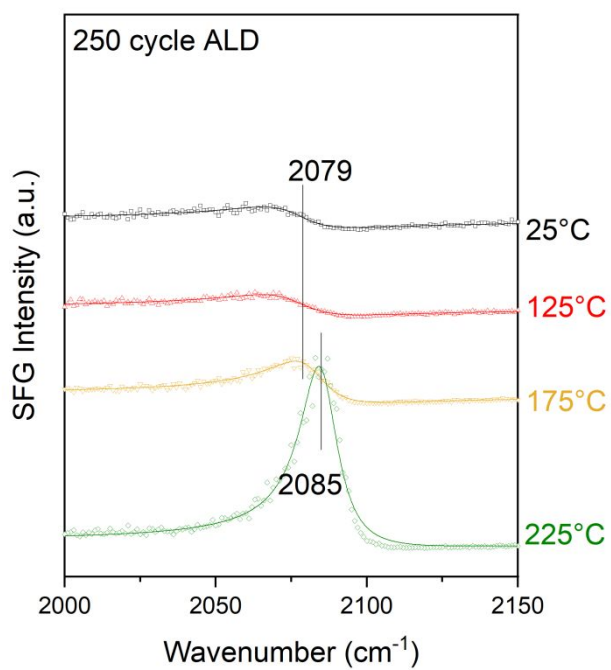


Figure S11: SFG spectra of the 250 cycle ALD Pt film previously exposed to 10 mbar CO at 275 °C and cooled down. Upon heating in 10 mbar CO and 20 mbar O<sub>2</sub>, the on-top CO peak was recovered at 225 °C.

## 4. DFT calculations

### 4.1 Computational method

Density Functional Theory (DFT) is used within the generalized gradient approximation using the plane-wave Vienna ab-initio simulation package (VASP)<sup>15-18</sup>. The calculations are performed using the PBE<sup>19</sup> exchange-correlation functional. The interaction between valence electrons and core is described using the projector-augmented wave (PAW) scheme<sup>20, 21</sup>. Carbon, oxygen and platinum are described with four, six and ten valence electrons, respectively. Integration over the Brillouin zone is approximated by finite sampling using the Monkhorst-Pack scheme<sup>22</sup>. k-point sampling corresponding to a (8x8x1) grid in a (2x2) surface cell for Pt(100) is used for all considered surface cells. A plane-wave cutoff of 450 eV is used. Slabs with four atomic layers are used to represent surfaces where the two bottom layers are kept fixed to their bulk positions during structural optimization. The structures are considered to be converged when the largest force is smaller than 0.05 eV/Å. The construction of the surface models is done using the atomistic simulation environment (ASE)<sup>23</sup>, whereas structural optimization and vibrational calculations are performed using the VTST tools<sup>24</sup>.

The adsorption energy of the adsorbates is calculated as:

$$E_{ads} = \frac{1}{N_{ads}} [E_{ads/slab} - E_{slab} - N_{ads}E_{ads}(g)]$$

where  $E_{ads/slab}$ ,  $E_{slab}$  and  $E_{ads}(g)$  are the total energies for the slab with the adsorbate, the bare slab and the gas phase molecule, respectively. The energies of gas-phase molecules are calculated in a cubic cell with a side of 15 Å.

The climbing image nudged-elastic band (CI-NEB) algorithm<sup>25</sup> as implemented in the VTST tools, is used to obtain the reaction barriers for CO dissociation, with the same force convergence criterion as for the geometry optimization. Frequency analysis is performed to

confirm that each transition states has only one single imaginary frequency in the direction of the reaction coordinate.

To compare the stability of systems with different CO coverage, we calculated the Gibbs free energy of adsorption at different coverages, using *ab-initio* thermodynamics<sup>26</sup>. The Gibbs free energy is given by:

$$\Delta G = \frac{1}{A} [N_{ads} E_{ads} - \mu_{CO} N_{ads} - N_{ads} T S_{vib}]$$

$N_{ads}$  is the number of adsorbed molecules,  $E_{ads}$  is the average adsorption energy,  $\mu_{CO}$  is the chemical potential of gas phase CO and  $S_{vib}$  is the vibrational entropy of the adsorbate. The chemical potential for CO is given by:

$$\mu_{CO}(T, p) = \mu'_{CO} + k_B T \ln \left( \frac{p_{CO}}{p^0} \right)$$

$\mu'_{CO}$  is the chemical potential at standard conditions, which is taken from a thermodynamic table<sup>27</sup>.

#### 4.2 CO dissociation over Pt(111), Pt(100) and Pt(211)

It is known that gradient corrected functionals, such as PBE do not reproduce the experimentally observed adsorption site for CO on Pt(111), which is on-top<sup>28</sup>. From the geometry of CO on Pt(111), we find that CO is preferably bonded in an fcc site with an adsorption energy of 1.76 eV. C and O are also preferably bonded in the fcc position, with adsorption energies of 7.14 eV and 1.19 eV, respectively. (The adsorption energy for O<sub>2</sub> is given with respect to O<sub>2</sub> in the gas phase, whereas the adsorption energy for C is with respect to the gas phase atom.)

On Pt(100), CO and O prefer to adsorb in bridge positions, with adsorption energies of 2.11 eV and 1.20 eV respectively, whereas C prefers the hollow position with an adsorption energy of 7.80 eV. These adsorption energies are in good agreement with a previous report<sup>29</sup>.

The energetics of CO dissociation over Pt(111) and Pt(100) is shown in Fig. S12. All adsorbates are treated in the preferred adsorption sites. The results show that direct CO dissociation in the low coverage limit is strongly endothermic; the energy difference between adsorbed and dissociated CO is in both cases around 2 eV. The strongly endothermic reaction indicates that the activation barriers are high. We calculate the barriers to be 4.51 eV and 3.95 eV over Pt(111) and Pt(100), respectively.

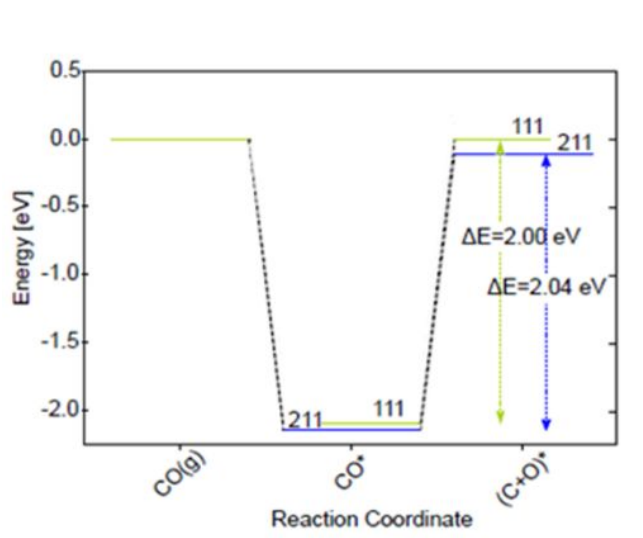


Figure S12. CO dissociation over Pt(111) and Pt(100). The reaction is studied in (2x2) surface cells.

In the literature, it has been reported that stepped Pt surfaces might reduce the barrier for CO dissociation<sup>30-34</sup>. To investigate dissociation over a step, we calculated CO dissociation over Pt(211). The reaction is in this case found to be endothermic by 2.04 eV. Thus, the barrier is at least 2.04 eV, which excludes direct CO dissociation as a possible path for the reaction.

Ways to obtain lower activation energies for CO dissociation are to stabilize the final state and/or destabilize the initial state. Stabilization of the final state can be done by formation of CO<sub>2</sub> through a Boudouard-like reaction, where two CO molecules on the surface react to give CO<sub>2</sub> and adsorbed C:



A similar reaction path was recently explored in Ref. <sup>35</sup> where CO dissociation was studied over Cu(211) forming CO<sub>2</sub> and a carbon-moiety. Following Ref.<sup>34</sup>, we reproduced the exothermic reaction pathway over Cu(211). However, the same reaction is strongly endothermic also over Pt(211). The optimized structures are shown in Fig. S13 with the relative energies for Cu(211) and Pt(211). The reason for the marked difference between Cu and Pt can be traced to the strong adsorption energy of C to four-fold hollow sites on Pt. The binding energy of C in the four-fold hollow sites on Pt surfaces is, in fact, comparable to the carbon stability in graphene.

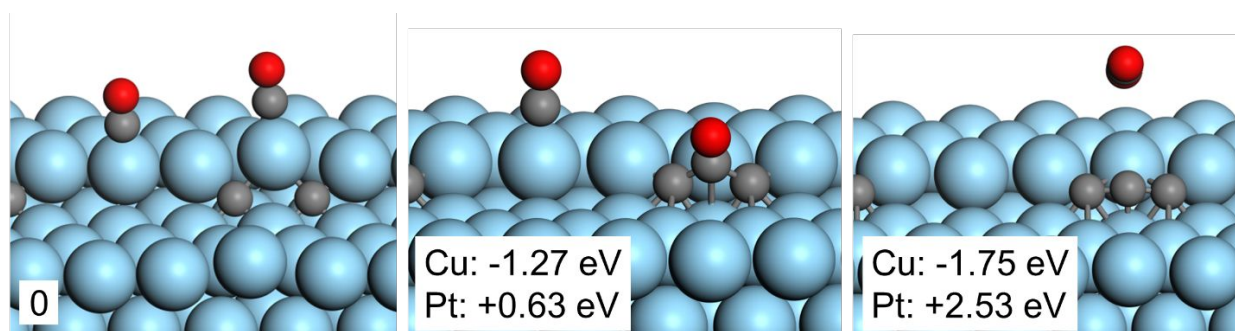


Figure S13. Structures for CO dissociation over Pt(211) forming CO<sub>2</sub> and a carbon moiety. The relative energy is given with respect to the left-most structure. Relative energies are also given for Cu(211) for comparison.

#### 4.3 CO dissociation over Pt-adatoms

It is known that CO adsorption can induce surface roughening<sup>36, 37</sup>, leading to special sites for CO adsorption and dissociation. Here we model such sites by Pt ad-atoms. The calculations were performed in a Pt(100) (2x2) supercell with the ad-atom placed in a hollow position. A thermodynamic analysis was performed to get the CO coverage at experimental conditions, see Fig. S14. At experimental conditions, we find that besides having two CO molecules adsorbed on the ad-atom, three CO molecules may be adsorbed on the terrace. This corresponds to a coverage of 1.25 with respect to the number of atoms in the (100) surface.

The barrier for CO dissociation through a Boudouard-type of mechanism is in this case calculated to be 1.82 eV. The corresponding structures are reported in the main text. The reaction is in this case endothermic by only 0.18 eV, which means that the increase in entropy while forming gas-phase CO<sub>2</sub> will drive the reaction.

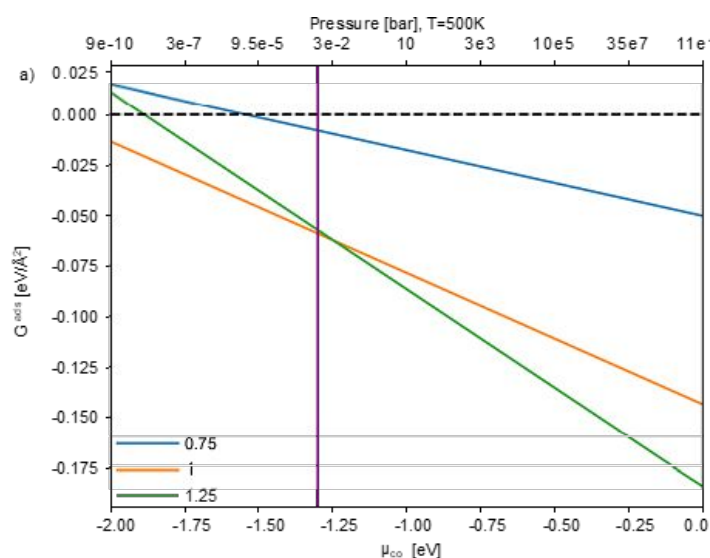


Figure S14. Thermodynamic analysis of CO adsorption over Pt-adatoms on Pt(100). Three different coverages are explored.

#### 4.4 CO dissociation over Pt(410)

As an additional model for rough Pt-surfaces, we investigated Pt(410). Pt(410) is chosen partly because of early attempts to elucidate CO dissociation over platinum<sup>38</sup>. The Pt(410) surface is treated in a (2x1) surface cell, which contains 10 surface atoms. The thermodynamic analysis (Fig. S15) shows that the coverage should be around 0.6 at the experimental conditions. The barrier for CO dissociation is in this case calculated to be 1.90 eV. The corresponding structures are shown in the main text. In similarity with the Pt ad-atom, the reaction is only moderately endothermic, and entropy will drive the reaction. We note that the barrier is sensitive to the CO coverage and a lower barrier can be obtained by increasing the coverage. In fact, a barrier of only 0.9 eV is calculated for the case with full (1.0) coverage.

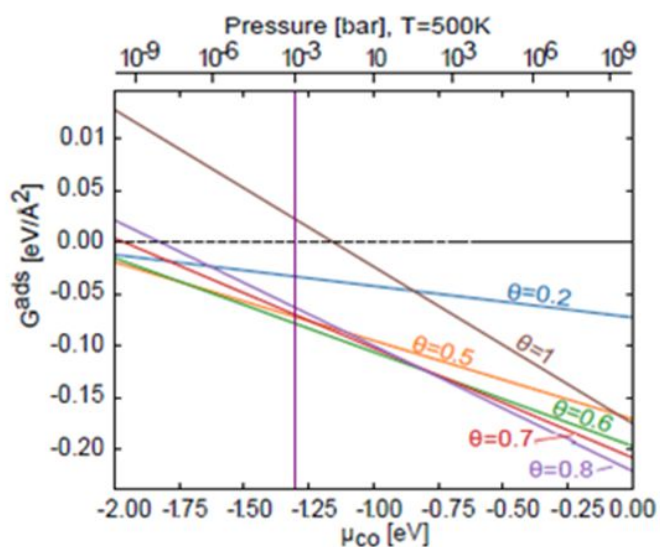


Figure S15. Thermodynamic analysis of CO adsorption over Pt(410). The structure is investigated for six coverages.

## 5. Measurements of CO oxidation

### 5.1 MS (and SFG)

In addition to the two samples shown in the main text, we investigated additional samples – the afore-mentioned 10 cycle sample and a 125 cycle sample, which represents a transition from particles to islands. The different response of all samples to temperature is shown in Table S2.

Table S2: Temperatures of disappearance of CO resonance in SFG spectra for different film thicknesses.

ALD Pt cycles	Absent CO peak in SFG at (°C)
250	400
125	425
50	450
10	475

Furthermore, to confirm that the reactivity results were reproducible and not influenced by the laser beam, repeated measurements with linearly ramped temperature were performed. Both previously discussed samples (250 and 50 cycle) were investigated. The initial gas phase again consisted of a 1:2 mixture of CO/O<sub>2</sub> with 10 mbar CO and 20 mbar O<sub>2</sub>. Alternatingly, the SFG lasers were on or off for each ramping cycle, with a ramping speed of 20 °C/min for the temperature increase. Figure S16 shows MS data for two temperature cycles with laser off (1 & 3) and laser on (2 & 4), both for the thicker ALD film and for the thinner film. No influence of laser irradiation was observed. These repeated measurements also indicate that no Pt sintering/morphology occurred upon reaction and repeated use, as the onset and size-dependence of SFG spectra did not change.

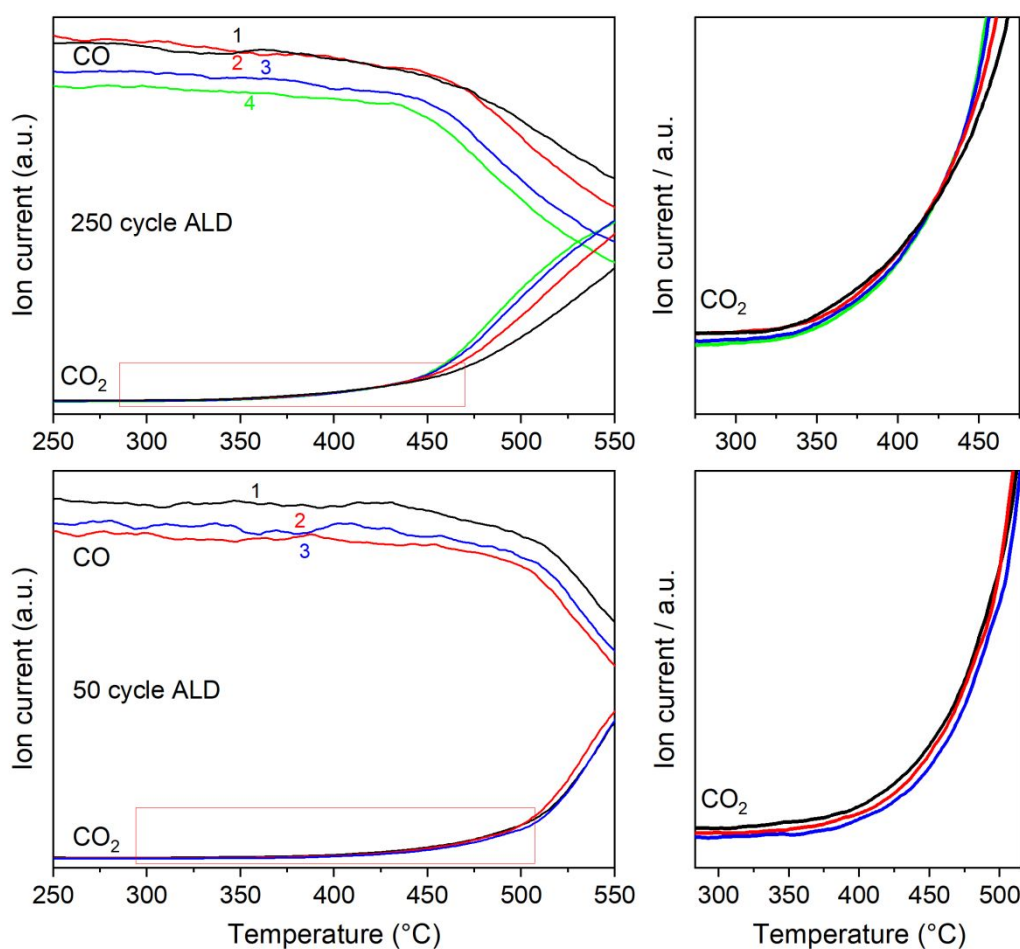


Figure S16: Mass spectrometer data for multiple cycles of CO oxidation on 250 cycle and 50 cycle ALD Pt in 1:2 mixture of CO/O<sub>2</sub> (batch mode; total pressure ~30 mbar). The right panels

are zoomed on the temperature at which CO oxidation starts. The measurements are alternating between temperature ramping with SFG lasers off (1,3) and SFG lasers on (2,4).

## 5.2 NAP-XPS and MS

XPS measurements were performed with a mixture of 1 mbar CO and 2 mbar O<sub>2</sub> under flow conditions. Figure S17 shows the XPS spectra of C 1s and Pt 4f, while increasing the temperature in steps of 25°C (for C1s) and 50 °C (for Pt 4f).

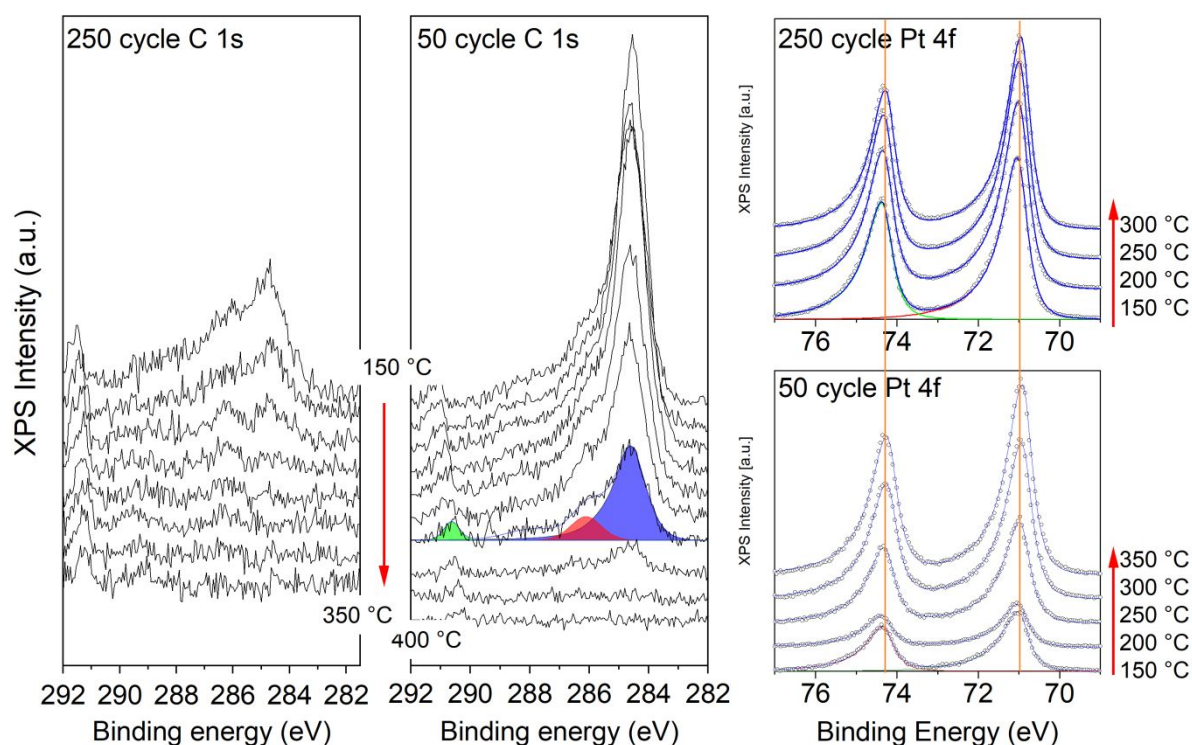


Figure S17: *In situ* NAP-XPS: Temperature evolution of C1s spectra for the 250 and the 50 cycle Pt film, in a reaction mixture of 1 mbar CO and 2 mbar O<sub>2</sub> (started at 150 °C and increased by 25°C steps). Graphitic carbon is marked in blue, adsorbed CO in red and gas phase CO in green. Corresponding Pt 4f XPS spectra of the 250 and 50 cycle film (1 mbar CO and 2 mbar O<sub>2</sub>) are shown on the right. It is clearly visible that the Pt signal is strongly dampened by the growing carbon film on the particulate 50 cycle Pt sample, before it is removed at higher temperature by oxidation.

The peak fitting was done in CasaXPS. For background subtraction Shirley backgrounds were used. For Pt asymmetric lineshapes (LF) were used with a splitting between the two peaks of 3,3 eV and an area difference of 4:3. For the graphitic carbon peak, an asymmetric lineshape (A) was used, whereas for the other C1s features symmetric lineshapes (GL) were applied<sup>39</sup>. The different contributions deduced from the spectra are shown in Fig. S18. The most important features were the graphitic carbon (at 284.5 eV) and adsorbed CO (at 286.2 eV), which consists of contributions of CO from different binding geometries, specifically terrace and step bound linear CO (see ref <sup>40</sup> for high resolution spectra of adsorbed CO on Pt). Figure S19 shows the evolution of these two peaks during heating and cooling of the samples in reaction mixture. The growth of the graphitic carbon due to CO dissociation is very pronounced on the 50 cycle rough Pt sample at low temperatures. A significant hysteresis of 50 °C is visible for both samples, i.e. during cooldown the reaction persists until lower temperature (the Pt surface remains CO-free).

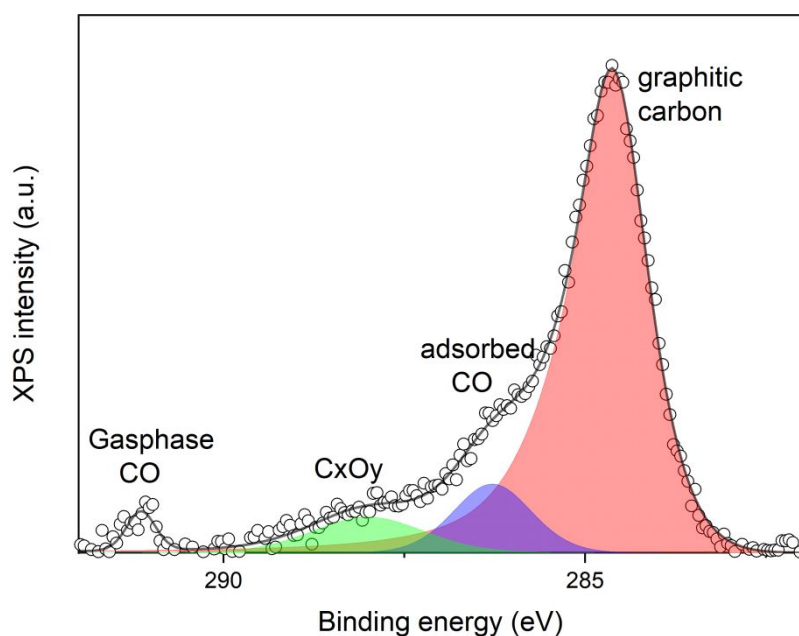


Figure S18: Example of peak fitting of C1s of 50 cycle ALD Pt film at 150 °C in 1 mbar CO and 2 mbar O<sub>2</sub>. At high binding energies, a CO gas phase peak is visible. The feature related to

surface species is composed of three single peaks of graphitic carbon, adsorbed CO and higher oxidized carbon species (carbonates on zirconia).

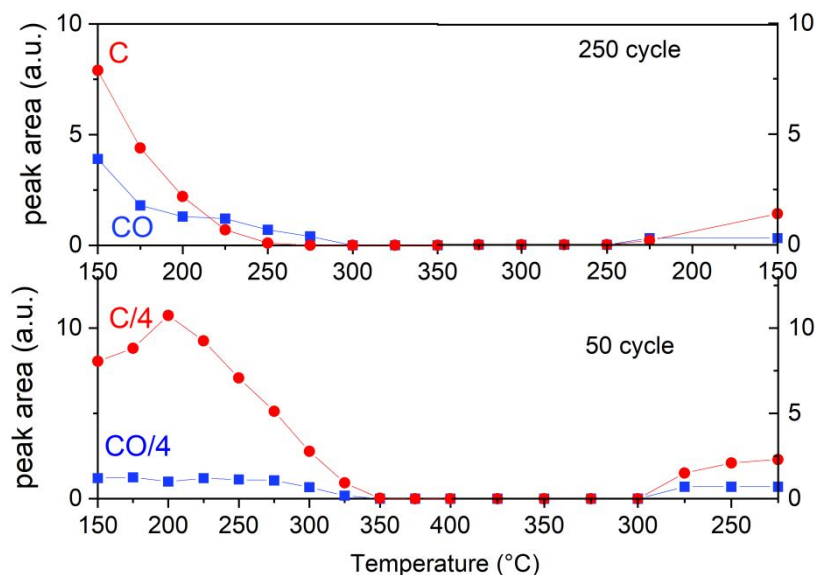


Figure S19: Quantified C and CO surface species from Fig. S17 upon heating up and cooldown (note the hysteresis): 250 (top) and 50 cycle (bottom) Pt film.

Fig. S20 shows MS data for the 50 cycle Pt film taken during the temperature steps of the NAP-XPS measurements, as well as the XPS peak intensities of gas phase and adsorbed CO. A direct correlation between the gas phase peak and the adsorbed CO peak is observed in the XPS measurements. This can be explained by the increase in  $\text{CO}_2$  in the production above 250 °C (see MS), inducing the strong decrease in (surface and gas phase) CO intensity in XPS.

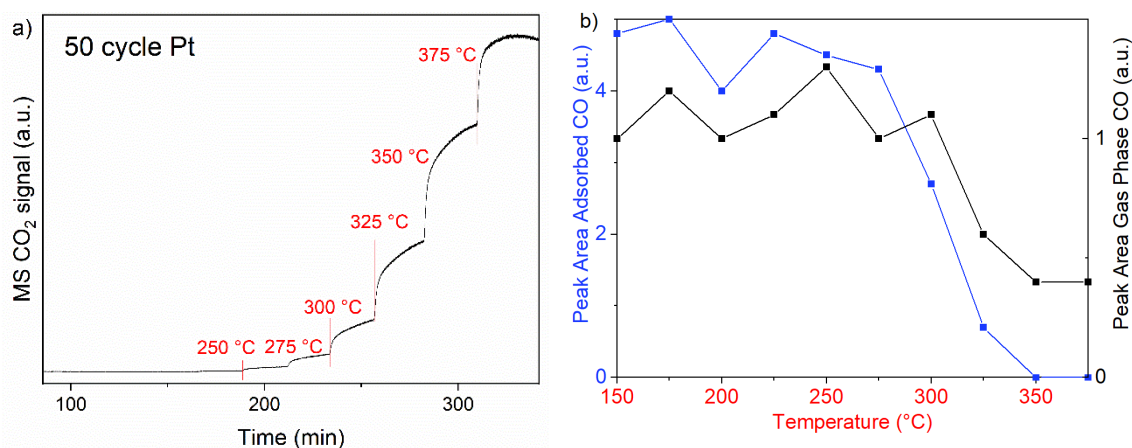


Figure S20: a) MS signal of CO<sub>2</sub> for the 50 cycle Pt film (flow mode; 1 mbar CO, 2 mbar O<sub>2</sub>). The temperature was stepwise increased during acquisition of XPS spectra. The respective temperatures are denoted in the plot. b) shows the XPS features of gas phase CO (black) and surface adsorbed CO (blue) for the same temperature steps. Above 275 °C, both peak areas drop significantly, correlated with the increase in CO<sub>2</sub> production.

1. Lu, J.; Elam, J. W.; Stair, P. C., Synthesis and Stabilization of Supported Metal Catalysts by Atomic Layer Deposition. *Acc. Chem. Res.* **2013**, *46* (8), 1806-1815.
2. Hausmann, D. M.; Kim, E.; Becker, J.; Gordon, R. G., Atomic Layer Deposition of Hafnium and Zirconium Oxides Using Metal Amide Precursors. *Chem. Mater.* **2002**, *14* (10), 4350-4358.
3. Aaltonen, T.; Ritala, M.; Tung, Y.-L.; Chi, Y.; Arstila, K.; Meinander, K.; Leskelä, M., Atomic layer deposition of noble metals: Exploration of the low limit of the deposition temperature. *J. Mater. Res.* **2004**, *19* (11), 3353-3358.
4. Rupprechter, G.; Dellwig, T.; Unterhalt, H.; Freund, H.-J., High-Pressure Carbon Monoxide Adsorption on Pt(111) Revisited: A Sum Frequency Generation Study. *J. Phys. Chem. B* **2001**, *105* (18), 3797-3802.

5. Shen, Y. R., Surface properties probed by second-harmonic and sum-frequency generation. *Nature* **1989**, 337 (6207), 519-525.
6. Li, X.; Roiaz, M.; Pramhaas, V.; Rameshan, C.; Rupprechter, G., Polarization-Dependent SFG Spectroscopy of Near Ambient Pressure CO Adsorption on Pt(111) and Pd(111) Revisited. *Top. Catal.* **2018**, 61, 751–762.
7. Lambert, A. G.; Davies, P. B.; Neivandt, D. J., Implementing the Theory of Sum Frequency Generation Vibrational Spectroscopy: A Tutorial Review. *Appl. Spectrosc. Rev.* **2005**, 40 (2), 103-145.
8. Wang, H.-F.; Gan, W.; Lu, R.; Rao, Y.; Wu, B.-H., Quantitative spectral and orientational analysis in surface sum frequency generation vibrational spectroscopy (SFG-VS). *Int. Rev. Phys. Chem.* **2005**, 24 (2), 191-256.
9. Roke, S.; Bonn, M.; Petukhov, A. V., Nonlinear optical scattering: The concept of effective susceptibility. *Phys. Rev. B* **2004**, 70 (11), 115106.
10. Roiaz, M.; Pramhaas, V.; Li, X.; Rameshan, C.; Rupprechter, G., Atmospheric pressure reaction cell for operando sum frequency generation spectroscopy of ultrahigh vacuum grown model catalysts. *Rev. Sci. Instrum.* **2018**, 89 (4), 045104.
11. Corva, M.; Feng, Z.; Dri, C.; Salvador, F.; Bertoch, P.; Comelli, G.; Vesselli, E., Carbon dioxide reduction on Ir(111): stable hydrocarbon surface species at near-ambient pressure. *Phys. Chem. Chem. Phys.* **2016**, 18 (9), 6763-6772.
12. Rameshan, C.; Li, H.; Anic, K.; Roiaz, M.; Pramhaas, V.; Rameshan, R.; Blume, R.; Hävecker, M.; Knudsen, J.; Knop-Gericke, A.; Rupprechter, G., In situ NAP-XPS spectroscopy during methane dry reforming on ZrO<sub>2</sub>/Pt(1 1 1) inverse model catalyst. *J. Phys. Condens. Matter* **2018**, 30 (26), 264007.

13. Ogletree, D. F.; Bluhm, H.; Lebedev, G.; Fadley, C. S.; Hussain, Z.; Salmeron, M., A differentially pumped electrostatic lens system for photoemission studies in the millibar range. *Rev. Sci. Instrum.* **2002**, *73* (11), 3872-3877.
14. Salmeron, M.; Schlögl, R., Ambient pressure photoelectron spectroscopy: A new tool for surface science and nanotechnology. *Surf. Sci. Rep.* **2008**, *63* (4), 169-199.
15. Kresse, G.; Hafner, J., Ab initio molecular dynamics for liquid metals. *Phys. Rev. B* **1993**, *47* (1), 558-561.
16. Kresse, G.; Hafner, J., Ab initio molecular-dynamics simulation of the liquid-metal--amorphous-semiconductor transition in germanium. *Phys. Rev. B* **1994**, *49* (20), 14251-14269.
17. Kresse, G.; Furthmüller, J., Efficiency of ab-initio total energy calculations for metals and semiconductors using a plane-wave basis set. *Comput. Mater. Sci.* **1996**, *6* (1), 15-50.
18. Kresse, G.; Furthmüller, J., Efficient iterative schemes for ab initio total-energy calculations using a plane-wave basis set. *Phys. Rev. B* **1996**, *54* (16), 11169-11186.
19. Perdew, J. P.; Burke, K.; Ernzerhof, M., Generalized Gradient Approximation Made Simple. *Phys. Rev. Lett.* **1996**, *77* (18), 3865-3868.
20. Blöchl, P. E., Projector augmented-wave method. *Phys. Rev. B* **1994**, *50* (24), 17953-17979.
21. Kresse, G.; Joubert, D., From ultrasoft pseudopotentials to the projector augmented-wave method. *Phys. Rev. B* **1999**, *59* (3), 1758-1775.
22. Monkhorst, H. J.; Pack, J. D., Special points for Brillouin-zone integrations. *Phys. Rev. B* **1976**, *13* (12), 5188-5192.

23. Bahn, S. R.; Jacobsen, K. W., An object-oriented scripting interface to a legacy electronic structure code. *Comput. Sci. Eng.* **2002**, *4* (3), 56-66.
24. Henkelman Group, The University of Texas at Austin. <http://theory.cm.utexas.edu/vtsttools/>.
25. Henkelman, G.; Uberuaga, B. P.; Jónsson, H., A climbing image nudged elastic band method for finding saddle points and minimum energy paths. *J. Chem. Phys.* **2000**, *113* (22), 9901-9904.
26. Reuter, K.; Scheffler, M., Composition, structure, and stability of RuO<sub>2</sub> as a function of oxygen pressure. *Phys. Rev. B* **2001**, *65* (3), 035406.
27. *NIST Chemistry WebBook, NIST Standard Reference Database Number 69*, Eds. P.J. Linstrom and W.G. Mallard. National Institute of Standards and Technology, Gaithersburg MD, 20899. <https://webbook.nist.gov/chemistry/> .
28. Feibelman, P. J.; Hammer, B.; Nørskov, J. K.; Wagner, F.; Scheffler, M.; Stumpf, R.; Watwe, R.; Dumesic, J., The CO/Pt(111) Puzzle. *J. Phys. Chem. B* **2001**, *105* (18), 4018-4025.
29. Trincherro, A.; Hellman, A.; Grönbeck, H., Methane oxidation over Pd and Pt studied by DFT and kinetic modeling. *Surf. Sci.* **2013**, *616*, 206-213.
30. Park, Y. O.; Masel, R. I.; Stolt, K., An XPS study of carbon monoxide and nitric oxide adsorption on platinum (410): Unusual dissociation activity. *Surf. Sci.* **1983**, *131* (1), L385-L389.
31. Park, Y. O.; Banholzer, W. F.; Masel, R. I., Platinum (410), a face with unusual activity for the breaking of N-O and C-O bonds. *Appl. Surf. Sci.* **1984**, *19* (1), 145-160.

32. Banholzer, W. F.; Parise, R. E.; Masel, R. I., Adsorption and interaction of CO and NO on Pt(410): II. Infrared studies. *Surf. Sci.* **1985**, *155* (2), 653-666.
33. McCrea, K. R.; Parker, J. S.; Somorjai, G. A., The Role of Carbon Deposition from CO Dissociation on Platinum Crystal Surfaces during Catalytic CO Oxidation: Effects on Turnover Rate, Ignition Temperature, and Vibrational Spectra. *J. Phys. Chem. B* **2002**, *106* (42), 10854-10863.
34. McCrea, K.; Parker, J. S.; Chen, P.; Somorjai, G., Surface structure sensitivity of high-pressure CO dissociation on Pt(557), Pt(100) and Pt(111) using sum frequency generation surface vibrational spectroscopy. *Surf. Sci.* **2001**, *494* (3), 238-250.
35. Ng, M. L.; Abild-Pedersen, F.; Kaya, S.; Mbuga, F.; Ogasawara, H.; Nilsson, A., Low Barrier Carbon Induced CO Dissociation on Stepped Cu. *Phys. Rev. Lett.* **2015**, *114* (24), 246101.
36. Roiaz, M.; Falivene, L.; Rameshan, C.; Cavallo, L.; Kozlov, S. M.; Rupprechter, G., Roughening of Copper(100) at Elevated CO Pressure: Cu Adatom and Cluster Formation Enable CO Dissociation. *J. Phys. Chem. C* **2019**, *123* (13), 8112-8121.
37. Haghofer, A.; Sonström, P.; Fenske, D.; Föttinger, K.; Schwarz, S.; Bernardi, J.; Al-Shamery, K.; Bäumer, M.; Rupprechter, G., Colloidally Prepared Pt Nanowires versus Impregnated Pt Nanoparticles: Comparison of Adsorption and Reaction Properties. *Langmuir* **2010**, *26* (21), 16330-16338.
38. Banholzer, W. F.; Park, Y. O.; Mak, K. M.; Masel, R. I., A model for the plane to plane variations in catalytic activity seen during nitric oxide decomposition on platinum. *Surf. Sci.* **1983**, *128* (1), 176-190.

39. van Attekum, P. M. T. M.; Wertheim, G. K., Excitonic Effects in Core-Hole Screening. *Phys. Rev. Lett.* **1979**, *43* (25), 1896-1898.
40. Tränkenschuh, B.; Fritsche, N.; Fuhrmann, T.; Papp, C.; Zhu, J. F.; Denecke, R.; Steinrück, H. P., A site-selective in situ study of CO adsorption and desorption on Pt(355). *The J. Chem. Phys.* **2006**, *124* (7), 074712.